SCIENTIFIC REPORTS

OPEN

Purkinje cell number-correlated cerebrocerebellar circuit anomaly in the valproate model of autism

Received: 8 October 2018
Accepted: 12 June 2019
Published online: 25 June 2019

Tamás Spisák[1,2], Viktor Román[1], Edit Papp[3], Rita Kedves[1], Katalin Sághy[1], Cecília Katalin Csölle[1], Anita Varga[1], Dávid Gajári[1], Gabriella Nyitrai[1], Zsófia Spisák[1], Zsigmond Tamás Kincses[1,4], György Lévay[1], Balázs Lendvai[1] & András Czurkó[1]

While cerebellar alterations may play a crucial role in the development of core autism spectrum disorder (ASD) symptoms, their pathophysiology on the function of cerebrocerebellar circuit loops is largely unknown. We combined multimodal MRI (9.4T) brain assessment of the prenatal rat valproate (VPA) model and correlated immunohistological analysis of the cerebellar Purkinje cell number to address this question. We hypothesized that a suitable functional MRI (fMRI) paradigm might show some altered activity related to disrupted cerebrocerebellar information processing. Two doses of maternal VPA (400 and 600 mg/kg, s.c.) were used. The higher VPA dose induced 3% smaller whole brain volume, the lower dose induced 2% smaller whole brain volume and additionally a focal gray matter density decrease in the cerebellum and brainstem. Increased cortical BOLD responses to whisker stimulation were detected in both VPA groups, but it was more pronounced and extended to cerebellar regions in the 400 mg/kg VPA group. Immunohistological analysis revealed a decreased number of Purkinje cells in both VPA groups. In a detailed analysis, we revealed that the Purkinje cell number interacts with the cerebral BOLD response distinctively in the two VPA groups that highlights atypical function of the cerebrocerebellar circuit loops with potential translational value as an ASD biomarker.

Autism spectrum disorder (ASD) is a lifelong neurodevelopmental disorder[1], currently diagnosed using behavioral tests that can be subjective; therefore, objective noninvasive imaging biomarkers of autism are being actively researched[2–5].

Cerebrocerebellar circuit dysfunction may play a crucial role in the etiology of ASD, as cerebellar lesions or structural and functional differences in various cerebellar subregions consistently have been linked to ASD[6–11]. MRI findings of the cerebellum in ASD, however, remain less clear[12]: although the size of the vermis appears to be slightly smaller and structural differences in cerebellar lobule VII (right crus I/II) are associated with core ASD symptoms and may have potential functional impact[6,7]. Similarly, the great majority of a substantial number of postmortem anatomical studies of ASD show decreased Purkinje cell density, but with focal regional alterations[6,13]. Furthermore, a distinct temporally regulated ASD gene module looks specific to developing Purkinje cells[14].

Neuroanatomical studies underline the extensive and region-specific connectivity between the cerebellum and the cerebral cortex with two-stage feed-forward and feed-back loops, e.g., lobules VI/VII (crus I/II) of the cerebellum are linked with the association areas of the cerebral cortex concerned with higher order behavior, such as the prefrontal cortex, posterior parietal cortex or cingulate gyrus[15,16]. The anterior part of the cerebellum has a sensory domain, in addition to its traditionally known role in motor functions, and the posterior part of it contributes to some aspects of affective and cognitive processing[17–19]. Indeed, cerebellar posterior lobe lesions define cerebellar cognitive affective syndrome, and *in utero* or early postnatal lesions induce behavioral and social deficits that overlap with ASD symptoms[16,20]. Finally, there is recent mechanistic evidence in mice showing that in juvenile life the chemogenetic perturbation of the activity of posterior vermal cerebellar regions specifically modulates the expression of ASD-related behaviors in adulthood[21].

[1]Pharmacology and Drug Safety Research, Gedeon Richter Plc., Budapest, Hungary. [2]Department of Neurology, University Hospital Essen, Essen, Germany. [3]Institute of Experimental Medicine, Hungarian Academy of Sciences, Budapest, Hungary. [4]Department of Neurology, University of Szeged, Szeged, Hungary. Tamás Spisák and Viktor Román contributed equally. Correspondence and requests for materials should be addressed to A.C. (email: czurkoa@richter.hu)

Despite these seminal findings highlighting the potential functional impact of disrupted cerebrocerebellar loops in ASD[8,22], fundamental questions about the pathophysiology of these cerebrocerebellar loops have remained unanswered. Equally, their translational utility is unknown, limiting the progress in pursuing objective neuroimaging biomarkers in ASD.

We addressed these questions by combining multimodal neuroimaging and correlated immunohistological analysis of the cerebellar Purkinje cell number in a prenatal rat valproate (VPA) model. We hypothesized that our functional MRI (fMRI) paradigm might show some altered activity related to disrupted cerebrocerebellar information processing. We used a somatosensory fMRI paradigm suitable for small animal imaging. Our paradigm, by involving nested loops of the whisker system at the cerebellar, midbrain and thalamocortical level[23], allocates reasonable translational power to sensory-attentional paradigms in human studies. To ensure that our findings are reproducible with a time window for potential pharmacological treatments, we performed an MRI assessment of the same cohort twice, with a one-month difference (measurement 1 and 2). Furthermore, in addition to a control group with maternal vehicle treatment, due to uncertainty regarding the optimal maternal VPA dose triggering changes in somatosensory fMRI activity and/or cerebellar alterations, we investigated two VPA groups, with maternal doses of 400 mg/kg and 600 mg/kg (hitherto referred to as the VPA400 and VPA600 groups).

Results

Valproate-induced reduction of cerebellar gray matter and whole brain volume. Because both human ASD and its VPA model are known to present specific morphological features, our first assessment was to perform volumetry and voxel-based morphometry (VBM) analysis on the structural MRI scans. Anatomical scans at measurement 1 revealed that prenatal exposure to VPA resulted in 3.2% smaller whole brain volume in the VPA600 group ($p = 0.006$, effect size: $-81.1\,mm^3$) compared to controls. Smaller brain size was also observed in gray matter (-3.2%, $p = 0.02$, effect size: $-52.7\,mm^3$) and white matter (-2.4%, $p = 0.09$, $-13.2\,mm^3$) volume; however, the latter was not significant. A milder difference in the whole brain volume (-2%, $p = 0.06$, effect size: $-51.9\,mm^3$) was observed in the VPA400 group, and this was not detectable either in the gray or in the white matter volume. Normalized gray and white matter volumes (calculated on the subject-level as percentage of the whole brain volume) were not different between groups. Detailed summary statistics of the volumetry data are listed in Supplementary Table 2.

VBM analysis of the structural MRI scans was used to localize the potential gray matter density differences. In the VPA600 group, the VBM analysis could not detect any well-localized source of the smaller global gray matter volume; there were no normalized voxels showing significantly lower gray matter density (signal intensity modulated by Jacobian determinants) compared to the vehicle group. On the other hand, significantly lower focal gray matter density was observed in the VPA400 group in various brainstem nuclei and the bilateral cerebellar crus II and paraflocculus compared to controls (Fig. 1). Comparing the VPA400 and VPA600 groups revealed localized focal cerebellar and brainstem gray matter alterations only in the VPA400 group, suggesting that this difference may specific to the 400 mg/kg prenatal dose. No positive differences in gray matter density were observed in either of the VPA groups compared to the VEH group (Supplementary Fig. 6).

BOLD response to whisker stimulation. We assessed the possible ASD-related functional changes in the VPA rat model in the sensory domain by somatosensory stimulation-based functional MRI. Whisker stimulation evoked a widespread, significant BOLD response in all three animal groups (Fig. 2A, Supplementary Fig. 6 and Tables 3–5). As expected, the activation peaked in the barrel field of the primary somatosensory (S1) cortex (contralateral to the stimulation side) and in a blob covering the primary auditory (Au1) and the secondary somatosensory (S2) cortices. The group-mean maximal signal change in S1 was 0.36%, 0.68% and 0.34% in the VEH, VPA400 and VPA600 groups, respectively. The ipsilateral somatosensory activation was weaker but also significant in all three groups. Additionally, bilateral striatal, frontal, orbitofrontal, insular, entorhinal, cerebellar, and amygdalar as well as brainstem (trigeminal) activations were found in all three groups. Local maxima and effect sizes are reported in Supplementary Tables 3–5. In general, group-level activation was the most extended in the VPA400 group ($455.8\,mm^3$), followed by the VPA600 ($225.2\,mm^3$) and the vehicle ($190\,mm^3$) groups.

Functional hyperactivation as a consequence of prenatal valproate exposure. Between-group fMRI analysis contrasts revealed that several of the striking differences of the groupwise activation patterns were statistically significant (Fig. 2B, Table 1). A remarkable and robust effect of prenatal VPA exposure was the widespread increase in the BOLD response to whisker stimulation (Fig. 2B, Table 1). In both the VPA400 and VPA600 groups, pronounced hyperactivation was found in the primary somatosensory, ventral orbital, anterior cingular and frontal association cortices.

Contrasting the VPA400 and VPA600 groups revealed stronger hyperactivation in the VPA400 group, especially in regions of the primary somatosensory (contralateral to stimulation), ventral orbital, and frontal association cortices (Table 1) but also in the cerebellar lobule VIII and crus II (Table 1).

Repeated MRI assessment of the functional and structural alterations. Measurement 2 (performed one month later) reproduced the results of measurement 1, indicating that most of our MRI findings persevered (Fig. 3C–F).

Despite the overall increase in the brain volume of all groups ($+3.2\%$, from $2564.8\,mm^3$ to $2646.4\,mm^3$ in the VEH group, see Supplementary Table 1), a 3.6% difference between the VPA600 and the VEH group still persisted ($p = 0.0007$, effect size: $-97.9\,mm^3$). This difference was also present in absolute gray matter volume (-3.3%, $p = 0.005$, effect size: $-54.5\,mm^3$). Normalized gray and white matter volumes (calculated on the subject-level as percentage of the whole brain volume) did not differ between groups.

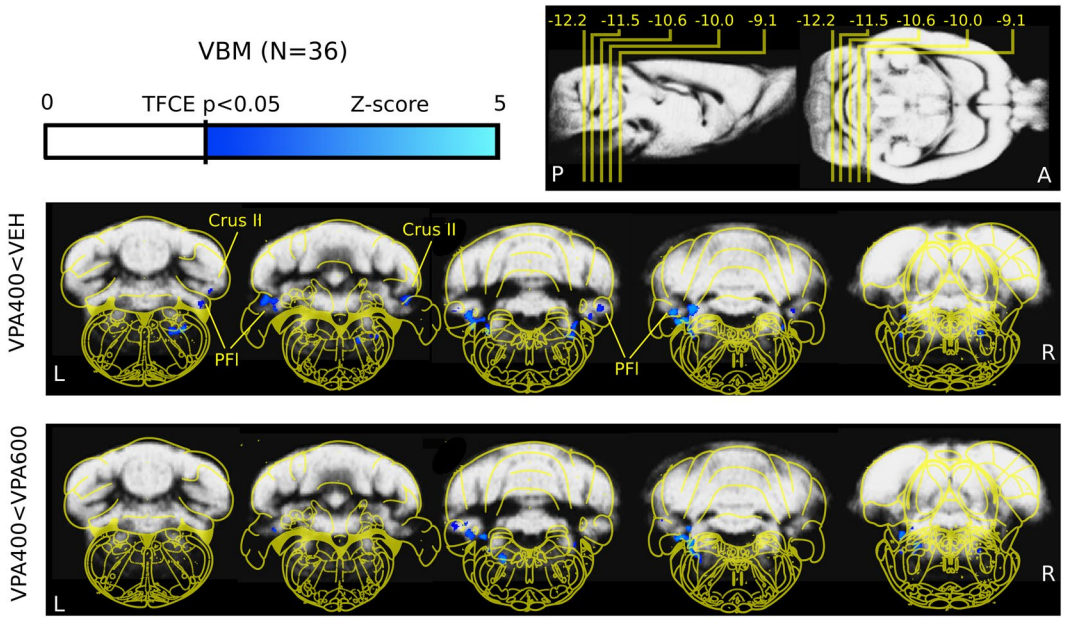

Figure 1. Decreased cerebellar and brainstem gray matter density revealed by voxel-based morphometry analysis. Evidence of cerebellar (crus II and paraflocculus) and brainstem (ventral nu. lat. lemniscus) lower focal gray matter density in the VPA400 group compared to both the VEH (top) and the VPA600 (bottom) groups (measurement 1). Compared to the VEH group, no decreases in VPA600 group and no increases in either of the VPA groups were observed. These results, together with the tissue volumetry analysis (Fig. 3), show that both VPA doses induced smaller whole brain volume while only the 400 mg/kg VPA dose induced detectable, focal localized cerebellar and brainstem gray matter alterations. On the top right of the figure, the position of slices (and their distance from bregma in mm) are shown on sagittal and horizontal planes. The colorbar represents Z-score (Gaussianized T-score) values of the parametric images (TFCE enhanced FDR-corrected significance threshold of $P = 0.05$). The slices highlight significant clusters (meaning that there are no significant changes in the cerebrum). Parametric images are overlaid on the study specific gray-matter probability map. Yellow overlay: Paxinos rat brain atlas. Images are shown in neurological convention (left-is-left; A: anterior, P: posterior, L: left, R: right; Crus II: crus II; PFI: paraflocculus).

The VBM analysis of measurement 2 demonstrated decreased gray matter density in cerebellar and brainstem locations of the VPA400 group with a remarkable overlap with measurement 1 (Fig. 3F). The decrease was also observed in contrast to the VPA600 group, while there was no change in gray matter density in any other group contrast.

In measurement 2, the group-level spatial pattern of whisker stimulation-induced BOLD activations were similar to those of measurement 1 (Supplementary Fig. 1.), although with smaller magnitudes due to the higher isoflurane doses. This and the smaller sample size due to exclusions (e.g., in-scanner motion; $N = 33$) resulted in a decreased statistical power. Nevertheless, we were still able to detect functional hyperactivation in the VPA400 group compared to the vehicle group. The hyperactivation was significant in a cluster in the primary somatosensory cortex (contralateral to stimulation, cluster-level correction for multiple comparisons, $P_{clust} = 0.045$, cluster-wise mean increase in effect size: 0.28%, see Supplementary Figs 2 and 3).

As mentioned above, due to the greater weight of the animals at measurement 2, more isoflurane was needed to maintain a comparable level of anesthesia and respiration rate (Supplementary Table 1). Since higher isoflurane doses dramatically affect neuronal activity and have vasodilatory action, these are unfavorable effects on the magnitude of BOLD responses[24]. Therefore, direct comparison or pooling of the measurements would be inappropriate and we regard measurement 2 merely as a confirmatory measure.

Decreased cerebellar purkinje cell number revealed by calbindin D28k immunostaining. Because lower Purkinje cell density is one of the most reproduced cerebellar postmortem anatomical findings in ASD, we made calbindin D28k (CB) immunostained sagittal sections from the cerebellar vermis of 27 rats (9 from each group). We found that the number of CB-positive Purkinje cells was significantly lower in both VPA groups compared to the VEH group (Fig. 4) in all lobules tested (6a, 6b, 6c, 7). The difference was a larger magnitude in the VPA400 group. All p-values were smaller than 0.005, implying very strong evidence of Purkinje cell loss. In all lobules, the magnitude of the Purkinje cell number decrease was stronger in the VPA400 group (−30.7%, −47.9% −29.2% and −32.6% in lobules 6a, 6b, 6c and 7, respectively) than in the VPA600 group (−21.4%, −19.5%, −26.3% and −24.3% in lobules 6a, 6b, 6c and 7, respectively). Staining intensity did not affect the quantification. Summary statistics of normalized Purkinje cell numbers found by calbindin D28k immunostaining are listed in Supplementary Table 6.

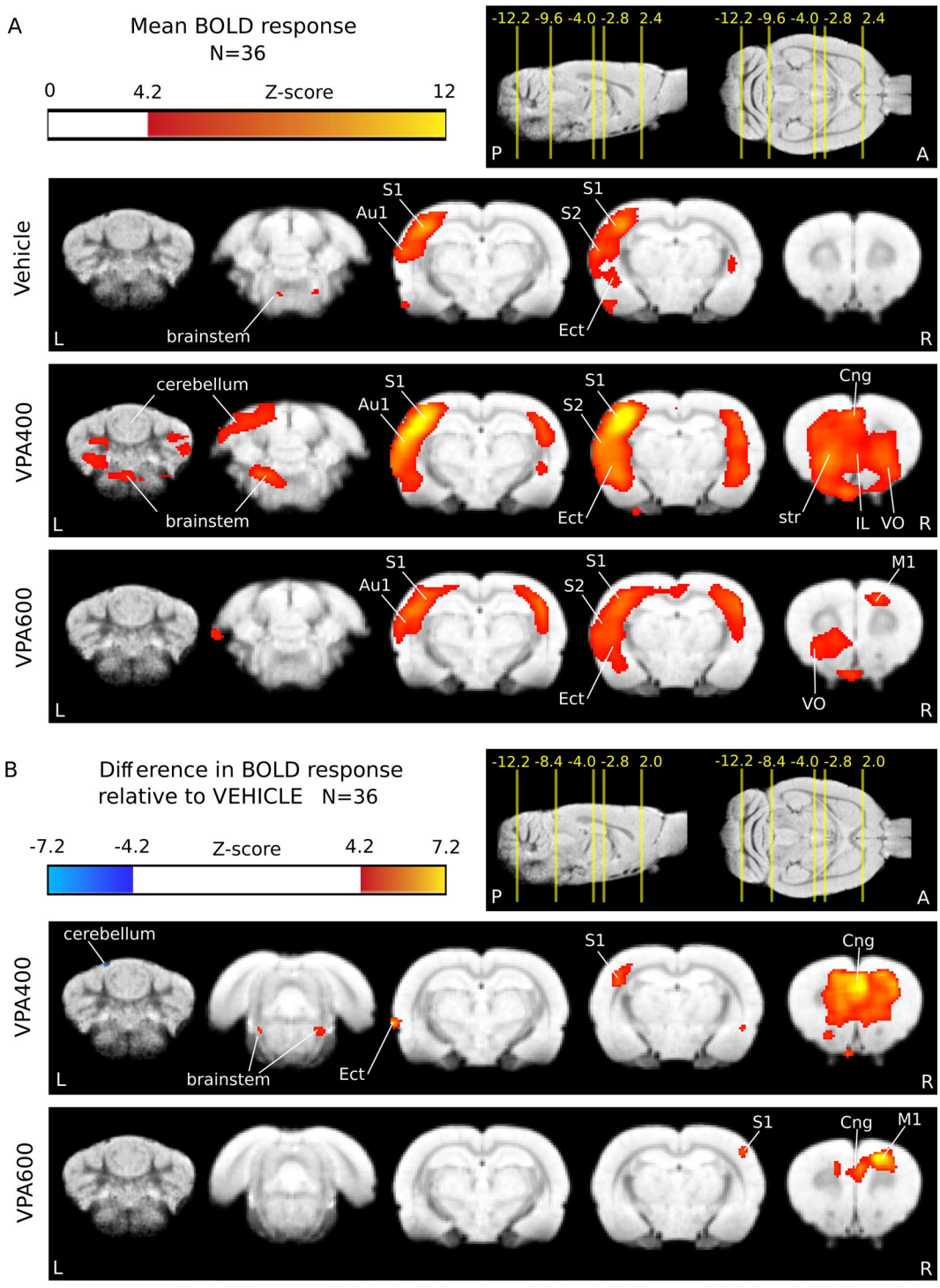

Figure 2. BOLD hyperactivation in response to somatosensory stimulation after prenatal valproate exposure. (**A**) Whisker stimulation triggered activation mainly in the contralateral primary and secondary somatosensory cortices (S1 and S2, respectively), auditory cortices (Au1) and the trigeminal nuclei of the brainstem. (**B**) BOLD response differences in the VPA400 and VPA600 groups compared to the VEH control group showed a robust activation increase in S1, anterior cingulate cortex (Cng), frontal areas (IL: infralimbic cortex, VO: ventral orbital cortex) and brainstem lateral lemniscus in the VPA400 group. A spatially restricted decrease was also observed on the cerebellar surface in this group. A similar but less prominent frontal and ipsilateral somatosensory hyperactivation was observed in the VPA600 group and involved the primary motor cortex (M1). Activations are displayed on coronal slices, overlaid on an in-house standard proton-density template. On the top right of each panel, the position of the slices are displayed on sagittal and horizontal planes as a distance from bregma in mm. Colorbars represent Z-score values. Significance thresholding was corrected for multiple comparisons ($P = 0.05$). Abbreviations: A: anterior, P: posterior, L: left, R: right.

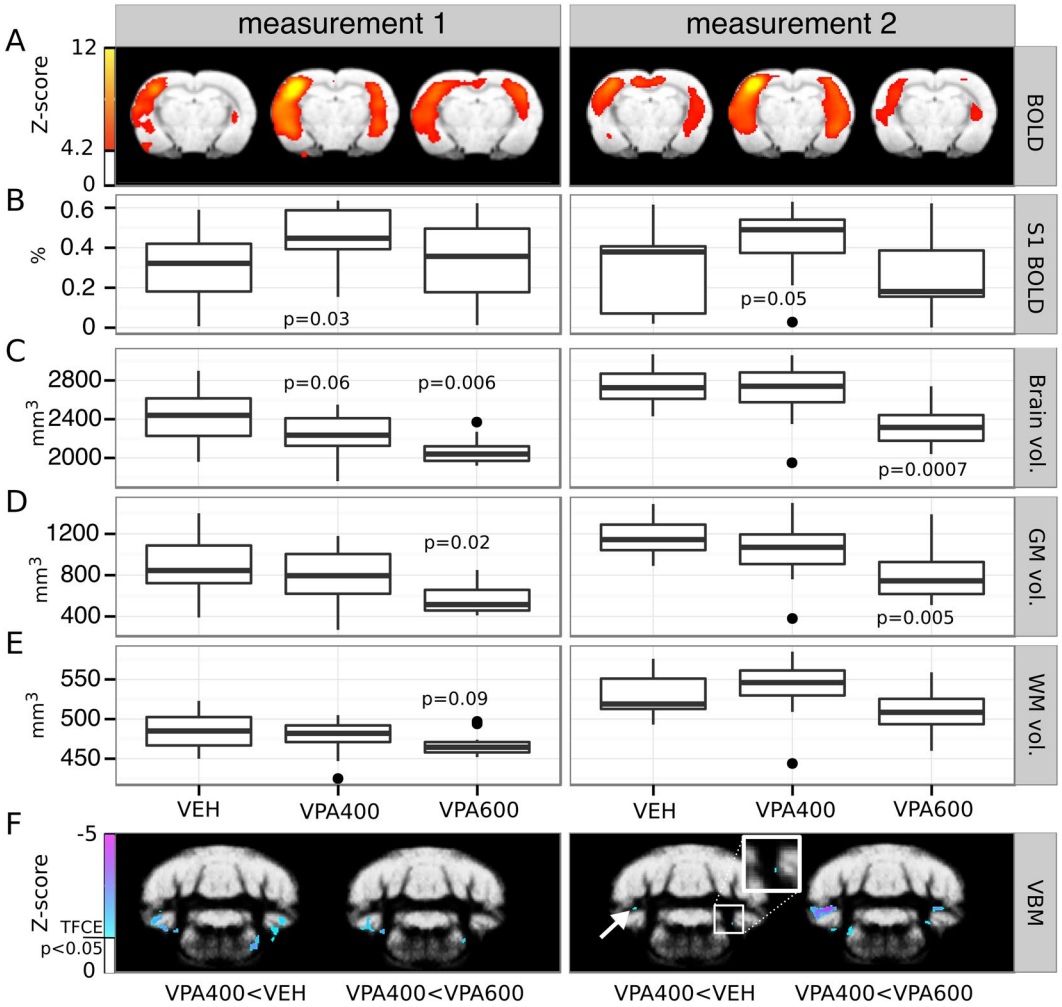

Figure 3. Persevered prenatal valproate-induced alterations demonstrated by a repeated MRI assessment of brain structure and function. (**A**) fMRI statistical parametric maps (at a coronal slice 2.8 mm from bregma in the posterior direction) of group-mean BOLD responses to whisker stimulation (right side) in the three experimental groups measured with one month difference. (**B**) Boxplots represent the average BOLD response in an unbiased somatosensory ROI (pooled-group mean activation Z-score > 9). Note the reproducible hyperactivation in the contralateral somatosensory cortex in the VPA400 group, in both measurements. (**C**,**D**,**E**) Boxplots depict the volume (mm^3) of the whole brain, gray matter and white matter, respectively. The VPA600 group exhibits a significantly decreased whole brain volume and gray matter volume in both measurements, despite the overall increase in brain volume. (**F**) Bilateral cerebellar and brainstem gray matter density decreases found by VBM in the VPA400 group compared to both the VEH group (left image in both panels) and the VPA600 group (right image in both panels), consistently in both MRI measurements. Inset zooms into small details of the image, revealing a spatially limited cluster of difference. Colorbars represent Z-score values. Statistical images are thresholded at a corrected threshold of FWER $P < 0.05$. Images are displayed in neurological convention (left-is-left). Boxes in the boxplots represent the 75th, 50th (median), and 25th percentile, whereas whiskers represent either the extrema or twice the interquartile range. Observations falling outside the 2*IQR range are represented by points. P-values lower than 0.1 (contrasting VPA groups to the VEH) are shown at the boxplots.

Correlation of the BOLD response with the cerebellar purkinje cell number. To the best of our knowledge, it is not known how lower Purkinje cell number is related to abnormal brain function in the VPA-model of ASD. Here, we analyzed how the correlation of individual Purkinje cell number and BOLD response to somatosensory stimulation is related to prenatal VPA exposure. In the VPA400 group (in animals with histological data available), a significant positive correlation of BOLD response with cerebellar Purkinje cell number was found in the frontal and cerebellar areas (Fig. 5B, Supplementary Table 10). In contrast, the VPA600 group exhibited a significant negative correlation in cortical and cerebellar regions (Fig. 5C, Supplementary Table 11). No significant correlation was found in the control group (Fig. 5A).

Interaction effect of cerebellar purkinje cell number and valproate treatment on the cerebellar and cerebral BOLD response. To capture VPA exposure-related effects, the differences in the group-wise "BOLD-Purkinje" correlation maps were further investigated by an interaction analysis. This revealed that

	x	y	z	% Signal change	Z-score	Region
VPA400 > VEHICLE	3.1	−0.4	−1.2	0.42	6.89	S1FL primary somatosensory cortex forelimb
	−1.5	3.2	−5.2	0.40	7.65	VO ventral orbital cortex
	−5.1	−3.0	−2.8	0.31	4.97	S1BF primary somatosensory cortex barrel field
	2.7	3.4	−4.4	0.29	6.68	LO lateral orbital cortex
	1.1	0.6	−2.2	0.28	5.81	Cg1 cingular cortex
	−7.7	−4.0	−6.8	0.20	6.83	Ect ectorhinal cortex
	2.1	4.8	−2.2	0.17	5.98	FrA frontal association cortex
	−4.5	0.8	−8.6	0.16	4.80	Pir piriform cortex
	2.9	2.8	−6.0	0.16	4.49	VO ventral orbital cortex
	2.3	1.0	−6.8	0.16	5.22	CPu striatum
	−2.7	−8.6	−7.6	0.15	4.75	brainstem (lateral lemniscus)
	−7.3	−3.4	−4.4	0.15	6.09	Au1 primary auditory cortex
	2.5	−8.2	−7.6	0.14	4.64	brainstem (lateral lemniscus)
	−7.7	−5.0	−7.4	0.12	4.41	Ect ectorhinal cortex
VPA600 > VEHICLE	2.5	−0.4	−1.2	0.51	6.91	S1HL primary somatosensory cortex hindlimb
	1.9	2.0	−2.4	0.35	7.47	M1 primary motor cortex
	3.3	2.4	−1.6	0.30	4.47	M1 primary motor cortex
	5.3	−2.8	−2.8	0.30	4.33	S1BF primary somatosensory cortex barrel field
	3.1	−0.6	−2.0	0.29	4.90	S1FL primary somatosensory cortex forelimb
	−0.9	−5.2	−6.0	0.23	4.31	thalamus
	−1.5	3.0	−6.2	0.22	4.71	VO ventral orbital cortex
	2.1	4.6	−2.2	0.15	4.44	FrA frontal association cortex
	−7.3	−3.4	−4.4	0.14	4.30	Au1 primary auditory cortex
	4.5	3.0	−5.8	0.06	5.01	AIV agranular insular cortex
VPA400 > VPA600	−5.1	−3.0	−2.8	0.37	5.55	S1BF primary somatosensory cortex barrel field
	1.1	4.4	−4.4	0.36	8.50	VO ventral orbital cortex
	−1.3	5.0	−2.4	0.24	4.78	FrA frontal association cortex
	5.1	1.4	−2.8	0.22	4.98	S1J primary somatosensory cortex jaw
	−7.7	−4.4	−6.8	0.20	6.17	Ect ectorhinal cortex
	3.7	−1.0	−5.2	0.19	4.58	CPu striatum
	−2.9	−8.8	−7.4	0.16	4.90	brainstem (lateral lemniscus)
	−0.5	−13.4	−5.4	0.14	5.05	lobule VIII cerebellum
	−2.7	−11	−7.4	0.14	4.48	brainstem (lateral lemniscus)
	−2.3	−14.0	−4.8	0.13	5.06	lobule VIII cerebellum
	−2.5	5.4	−2.6	0.12	4.46	FrA frontal association cortex
	2.3	−13.0	−6.2	0.11	4.30	crus II cerebellum
	4.7	−13.4	−6.2	0.10	4.50	crus II cerebellum
	3.7	3.8	−6.0	0.09	4.58	LO lateral orbital cortex

Table 1. Local maxima of the change of the fMRI BOLD response in the VPA400 and VPA600 groups compared to the VEH control group. Only local maxima above the FWER $P > 0.05$ threshold ($|Z| > 4.29$) are shown. The minimum peak distance is set to 3 mm. Peaks are listed by effect size (% BOLD signal change) in decreasing order. Coordinates are given relative to bregma, according to the atlas of Paxinos and Watson (x: medial-lateral, y: anterior-posterior, z: dorsal-ventral).

the regression slopes between BOLD response and Purkinje cell number in the medial frontal cortex and in a small cerebellar region are significantly larger in the VPA400 group than in the vehicle group (Fig. 5D). We also observed areas of significant interaction in the VPA600 group. Here, the interaction coefficient was negative, implying that the regression slopes between BOLD response and Purkinje cell number in some cerebellar and somatosensory regions are significantly smaller (in fact, more negative) in the VPA600 group than in the vehicle group (Fig. 5D). The significant cerebral interaction between VPA treatment and Purkinje cell number suggests a VPA-induced cerebrocerebellar malfunction that is unseen when only focused on the cerebellum.

To gain a more direct insight into the *treatment x Purkinje* interaction effect on BOLD response, we conducted an ROI analysis. We defined two unbiased ROIs and investigated the effect of cerebellar Purkinje cell number on the individual ROI-mean cerebellar and cerebral BOLD responses. Analysis of the cerebellar ROI (left part of Fig. 6) revealed a general positive correlation between cerebellar BOLD response and Purkinje cell number in the VEH group. No such correlation was observed in the VPA600 group; however, the values might represent the naturally continuing trajectory of the relationship seen in the VEH group, but in ranges of the lower Purkinje numbers, where the BOLD response already converges to zero. In contrast, the strong positive correlation in the

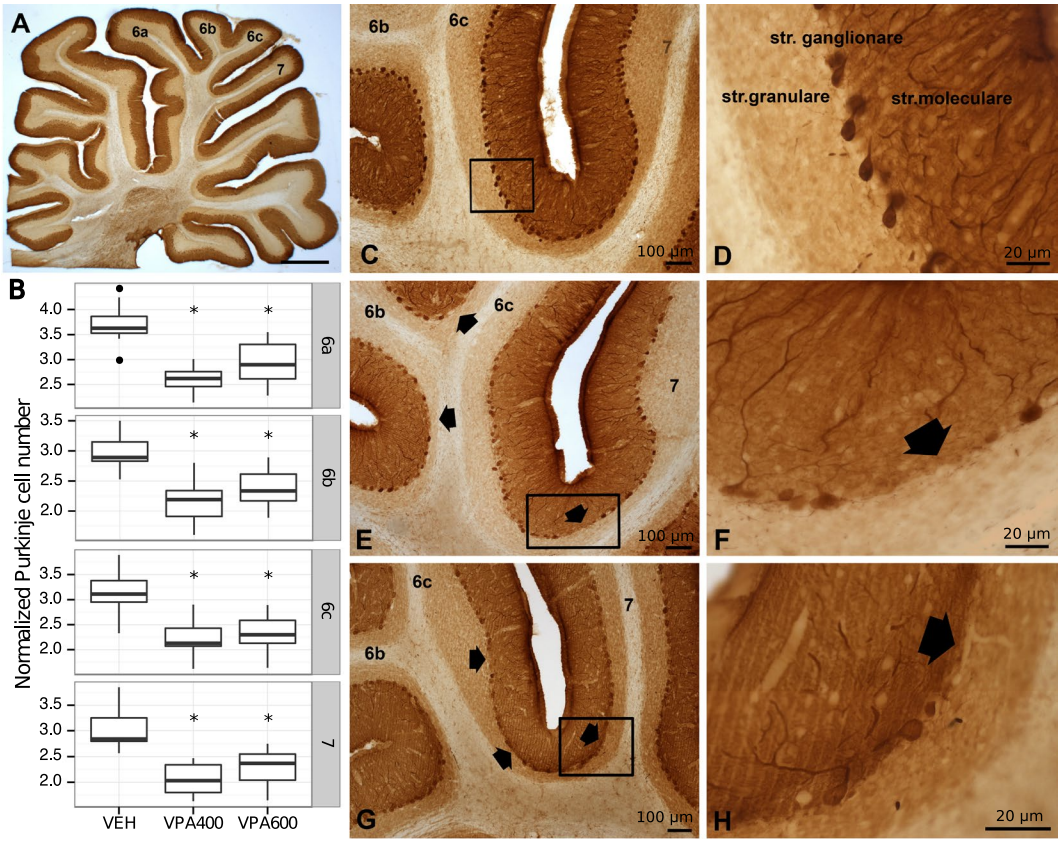

Figure 4. Prenatal valproate exposure induced reductions in cerebellar Purkinje cell number. (**A**) Light micrograph of calbindin D28k (CB) immunostained sagittal section of rat cerebellar vermis at low magnification. (**B**) Boxplots representing normalized CB immunoreactive Purkinje cell numbers in cerebellar vermal lobules 6a, 6b, 6c and 7, for the VEH, VPA400 and VPA600 groups. Asterisks depict significant ($p < 0.05$) decreases compared to the VEH group. (**C**,**D**) Normal distribution of CB immunoreactive Purkinje cells in the ganglionic layer of cerebellar cortex on VEH sections. (**E**–**H**) Decreased CB-positive Purkinje cell number, found both in the VPA400 and VPA600 groups. The arrows point to unlikely large areas with lack of Purkinje cells. Scale bars: 1000 μm (**A**), 100 μm (**C**,**E**,**G**), 20 μm (**D**,**F**,**H**).

VPA400 display no continuity to the VEH group. In this case, despite the remarkable decrease in Purkinje cell number, the BOLD responses were comparable to those of the controls.

In the cerebral activation areas (right side), both the VEH and the VPA600 groups exhibited a significant negative correlation between BOLD response and Purkinje cell number. However, this relationship became positive in the VPA400 group. The difference in slopes was captured by a significant interaction effect. Despite the lower BOLD responses due to anesthesia-related issues with larger animals, the second MRI measurement confirmed the tendency of a positive correlation between BOLD response and Purkinje cell number (Supplementary Fig. 5)

Discussion

Although autism has a strong genetic component, there are many cases of autism, termed "idiopathic", that are likely influenced by environmental factors[25]. Animal models of idiopathic ASD include either inbred rodent strains that mimic ASD behaviors or models developed by environmental interventions such as prenatal exposure to VPA[26]. This model of ASD exhibits face, construct and predictive validity and properly represents the epigenetic origin of idiopathic ASD[27,28]. While a few reports have already examined cerebellar anomalies in the prenatal VPA rodent model[29–32], the relationship of the abnormal Purkinje cell number to the function of cerebrocerebellar circuitry has not yet been investigated.

ASD-like cerebral and cerebellar structural changes. In our study, brain volume decrease was globally detected in the VPA600 group. In preclinical studies, even higher prenatal dose regimens are often used with similar results[30,33]; however, the observed magnitude of whole brain volume differences might be somewhat severe. On the other hand, in case of the smaller dose (VPA400 group), beside milder brain volume decrease, focal, cerebellar gray matter differences were detected (Fig. 1) which might be an autistic-like morphological feature. These morphometric alterations localized in the cerebellar crus II and paraflocculus (in both measurements) compared to the VEH control group and the VPA600 group. The paraflocculus could be involved in atypical gaze[34], the posterior cerebellar vermis (vermal lobules VI-VII) in repetitive behaviors and stereotyped interests in ASD[35].

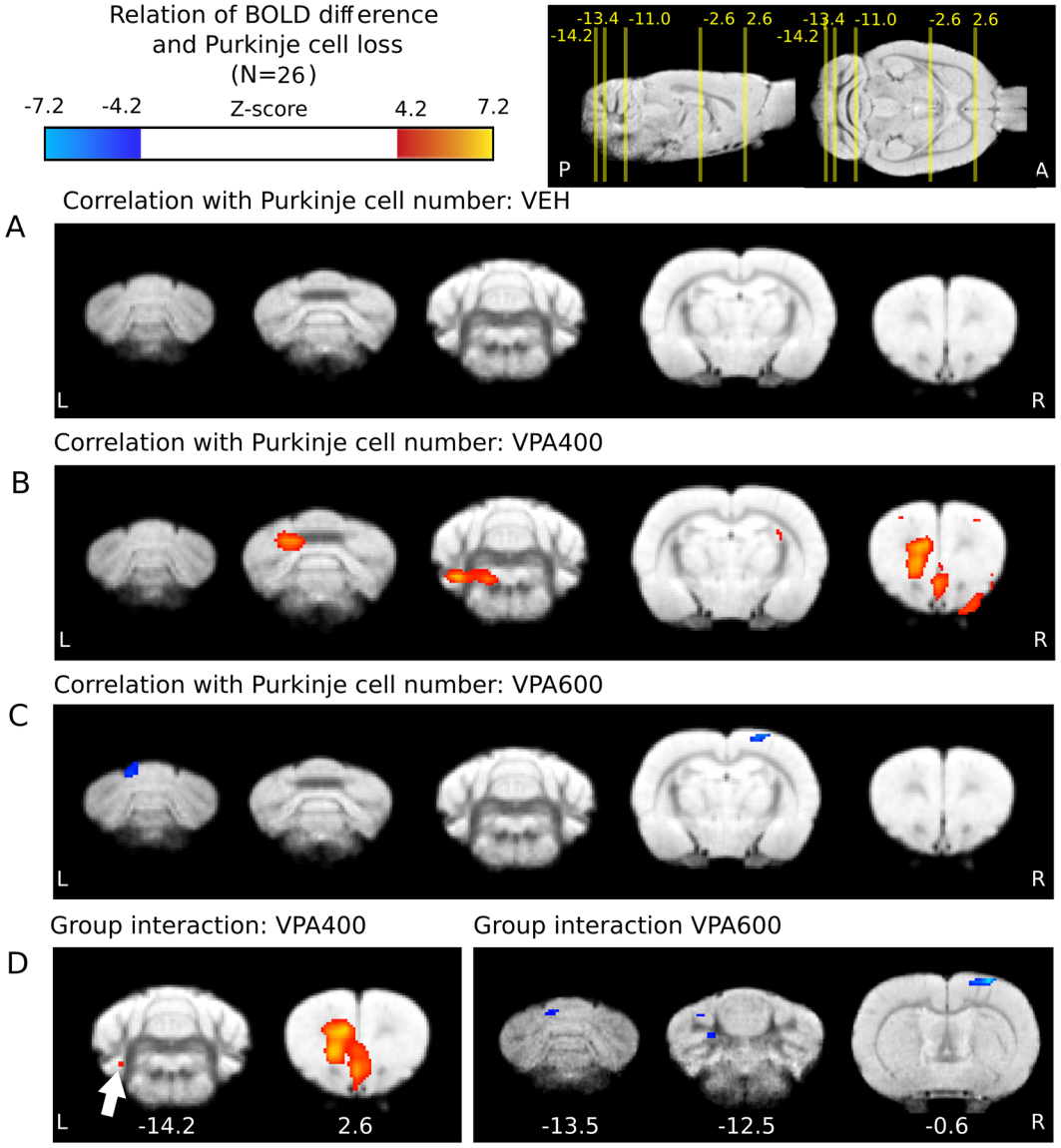

Figure 5. Prenatal valproate changes in the correlation of BOLD response and Purkinje cell number are present in both the cerebellum and the cerebral cortex. (**A**) No significant correlation of BOLD response (from measurement 1) with Purkinje cell number in the control group. (**B**) Significant positive interrelationship in the frontal and cerebellar areas in the VPA400 group. (**C**) Negatively correlated cortical and cerebellar regions with Purkinje cell number in the VPA600 group (**D**) Significant interaction effect between Purkinje cell number and treatment group on the BOLD response in a frontal and a cerebellar region of the VPA400 group (left side) and in somatosensory and cerebellar regions of the VPA600 group. Compared to controls, red indicates a greater regression slope in the VPA400 group, and blue denotes a lower slope in the VPA600 group. The distance of slices from bregma are shown under the slices. For effect sizes, see Supplementary Tables 12 and 13. Activations are displayed on coronal slices, overlaid on an in-house standard proton-density template[62]. On the top right, the positions of the slices are shown on sagittal and horizontal planes as a distance from bregma in mm. Colorbars represent Z-score values. Significance thresholding was corrected for multiple comparisons ($P = 0.05$). Abbreviations: A: anterior, P: posterior, L: left, R: right.

Crus I/II abnormalities are related to more severe ASD impairments in all domains[7] with altered functional connectivity to specific cerebral regions[11,36,37].

Our structural MRI findings in this model are in line with similar studies on absolute brain mass in early postnatal life, demonstrating reduced brain mass after 500 mg/kg VPA exposure[38], and microencephaly (on E14 and E18) followed by macroencephaly (on P2 and P7) after 400 mg/kg VPA exposure[39]. Several human studies have suggested divergent age effects on brain morphology changes in ASD[40], with a more rapid age-related cortical thinning in temporal and parietal regions compared to controls[41]. Decreased thickness in the temporal cortex was reported recently from a large multinational sample of the ENIGMA ASD working group, while at the same time, increased cortical thickness in the frontal cortex was found[42]. Similarly, using data from the multicenter

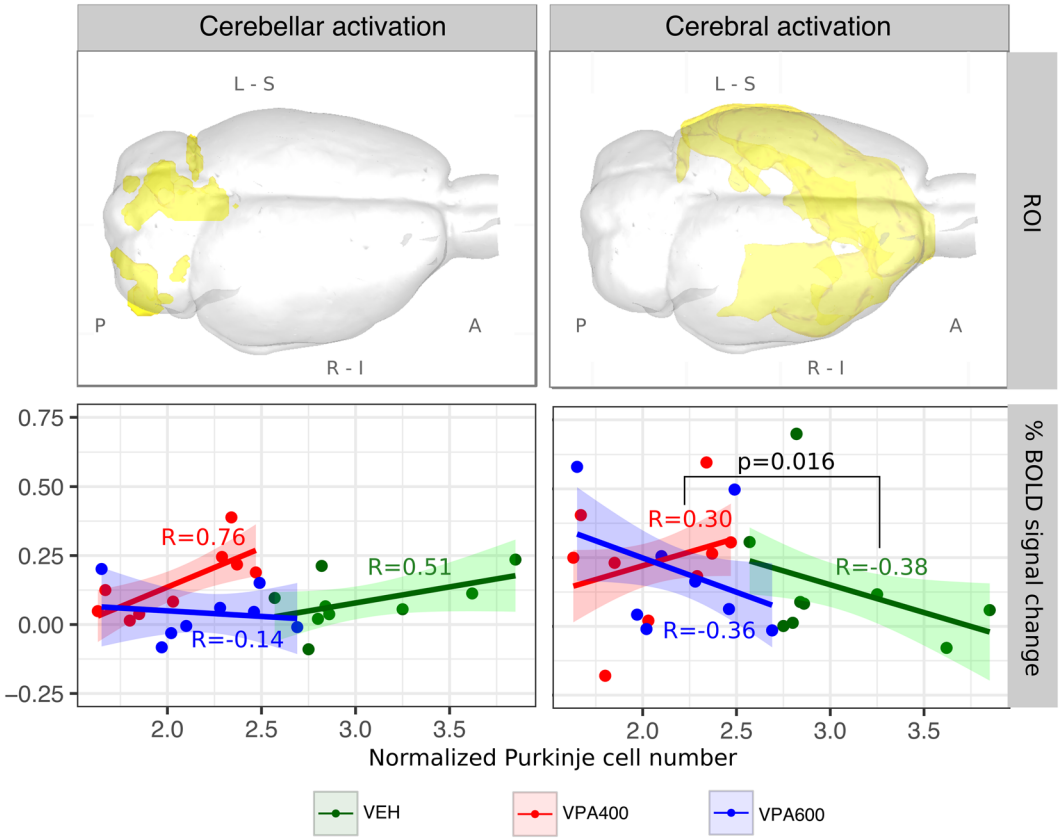

Figure 6. Atypical relationship between BOLD response and Purkinje cell number in cerebellar and cerebral ROIs of the pooled activation maps, suggesting probable malfunction of reciprocal cerebrocerebellar circuits. ROIs (visualized in 3D glass-brains) were defined based on the F-contrast representing the unbiased, pooled activation map, thresholded at FWER $p < 0.05$ and divided into cerebellar (left) and cerebral (right) components. Analysis of the cerebellar ROI (left column) revealed a general positive correlation between frontal BOLD response and Purkinje cell number in the VEH group. No such correlation was observed in the VPA600 group. Despite the remarkable decrease in Purkinje cell number in the VPA400 group, BOLD responses, in terms of both magnitude and correlation with Purkinje cell number, were comparable to those of the controls. In the cerebral ROI (right panel), both the VEH and the VPA600 groups exhibited a significant negative correlation between BOLD response and Purkinje cell number. Interestingly, the correlation was positive in the VPA400 group, which possibly indicates the presence of an atypical cerebrocerebellar circuit in this VPA group. Abbreviations: A: anterior, P: posterior, L: left, R: right, S: superior, I: inferior.

repository, the ABIDE initiative, a surface-based cortical thickness analysis revealed an increase in prefrontal cortical thickness in ASD[43]. Remarkably, an inverse correlation had been found earlier between the sizes of the frontal lobe and cerebellum in ASD[44], reflecting an abnormal overgrowth in the frontal lobes[45].

Sensory BOLD hyperactivation induced by prenatal valproate exposure. Sensory abnormalities are known in ASD (DSM-5, diagnostic criteria B.4.) Somatosensory evoked potentials show hyperactivity in infantile autism[46] as in Fmr1(−/y) mice[47]; therefore, sensory hypersensitivity may have translational value. Prenatal VPA rats have also shown increased sensory reactivity to mechanical stimuli[48] and increased neuronal activation in the auditory brainstem after sound exposure[49]. Interestingly, local functional overconnectivity was not demonstrated in the somatosensory cortex of ASD individuals by magnetoencephalography, challenging the theory that the primary substrate of hypersensitivity is localized in the somatosensory cortex[50].

In our fMRI measurement, the presence of altered sensory processing was reinforced in the prenatal VPA model of autism. The BOLD hyperactivation was more pronounced in the VPA400 group, but it was also clearly present in the VPA600 group. BOLD hyperactivation was prominent in areas with a significant group-mean response in the VEH group, and frontal hyperactivation, including the lateral and ventral orbital, prelimbic, frontal association, and anterior cingular cortices, was also found in the VPA groups. In the VPA400 group, there were additional activations in the brainstem (lateral lemniscus) and cerebellar regions (specifically in the crus II); however, these cerebellar activations proved to be significant only when compared to the VPA600 group.

Although both the morphometric alterations found in our VBM analysis and the cerebellar hyperactivations in the VPA400 group were localized in nonsensorimotor areas of the cerebellum (paraflocculus and crus II), a direct link of structural changes to the observed sensory hyperactivation might also be possible, since there

is evidence for a noncanonical organization of cerebrocerebellar circuits in ASD, especially in the sensory domain[51,52]. Since the paraflocculus has projections to the brainstem and the crus II normally interconnects with frontal and parietal areas, the brainstem (lateral lemniscus) and frontal components of the BOLD hyperactivation might also reflect the consequences of noncanonically organized cerebrocerebellar circuits. Consistent with this interpretation, abnormal cortical connectivity of the crus I/II region has been found in ASD[7,8,11].

Atypical effect of decreased Purkinje cell number on cerebrocerebellar activity. Following current ideas about the atypical functional connectivity of cerebrocerebellar circuit loops in ASD[7,8,51–54], it is straightforward to hypothesize that the significant VPA-induced decrease in Purkinje cell number might have a developmental effect on the cerebral cortical regions the cerebellum functionally connected with[8,22]. We addressed this assumption by testing the groupwise correlation of BOLD response and Purkinje cell number and whether it was different between groups (evaluating the "*treatment x Purkinje cell number*" interaction effect on the BOLD response).

In the case of the cerebellar BOLD signal, the main contributor to the activity is the parallel/mossy fiber system[55], and the contribution of the Purkinje cell activity might be relatively small[56]. Therefore, instead of simply reflecting the summed activity of Purkinje cells, the positive correlation between BOLD response and Purkinje cell number observed in the control group might be driven by the indirect effect of increased cerebral input through the parallel/mossy fiber systems.

On the other hand, throughout the cerebral activation areas, the BOLD - Purkinje cell number correlation is negative in the control group, which might be either a consequence of a stronger modulatory/inhibitory effect in the presence of more Purkinje cells or might be caused by some neurodevelopmental source affecting both Purkinje cell development and the maturation of distant cerebral circuits. Indeed, on the Purkinje cell level, prenatal VPA exposure delayed the developmental excitatory/inhibitory GABA "switch"[57], supporting a role of developmental timing in the pathophysiology of ASD.

The correlation of the BOLD response and Purkinje cell number is strongly dependent on the dose of VPA exposure. The simplest explanation for the significant "*group x Purkinje cell number*" interaction in the VPA600 group is that they represent a naturally continuing, nonlinear trajectory of the VEH group but in ranges of significantly lower Purkinje cell numbers, where the BOLD response already saturates to zero (thereby introducing a difference in linear regression slopes; also visible in Fig. 6). However, this explanation does not hold for the VPA400 group. Here, our results suggest that, despite the lower Purkinje cell numbers, the BOLD-Purkinje correlation maintained at similar or even higher levels than those of the control group, possibly by means of some compensatory mechanisms. Importantly, this "compensated" cerebellar BOLD response is accompanied by an atypical effect on cerebral responses, where the BOLD-Purkinje correlation turns from negative to positive. Notably, the atypical BOLD-Purkinje correlation is most pronounced in the frontal activation areas, supporting our hypothesis that noncanonically organized cerebrocerebellar circuits are present between the crus II and frontal regions. This might be a sign of a drastic VPA-related change in cerebrocerebellar modulation and/or a consequence of VPA-induced developmental diaschisis[22]. While the underlying mechanism remains unclear, our results demonstrate that measurable correlations exist in the VPA model between the cerebellar morphology and cerebrocerebellar circuit loop function.

Limitation of the study. In order to avoid interference between behavioral testing and MRI measurements, the ASD-like phenotypes were not assessed in the same rats involved in the MRI study. Although the compatibility to ASD-like phenotypes in the different rodent VPA models was reviewed recently[58], data from ASD-related behavioral tests measured in a cohort reared independently from the MRI cohort are provided in the Supplementary Material (Supplementary Figs 7–9). In these tests both VPA400 and VPA600 rats had unaffected spontaneous locomotor activity, while both VPA groups were impaired in the social novelty test. Interestingly only the VPA400 group exhibits alteration in juvenile social play test at postnatal day 33-36 (Supplementary Fig. 8).

Conclusion

In this multimodal MRI study of the VPA rat model of ASD, we found (i) ASD-like global and cerebellar changes in brain morphology, (ii) a functional BOLD hyperactivation to whisker sensory stimuli and (iii) distinct correlations between the cerebellar Purkinje cell number and cerebral BOLD responses in the two VPA groups. Our results suggest an altered interaction between the cerebellar and frontal cerebral areas. These alterations in the rat VPA model of ASD have potential translational value in the search for objective neuroimaging biomarkers in ASD.

Methods

Subjects. Timed-mated female Sprague-Dawley rats (Harlan, San Pietro al Natisone, Italy) arrived at the local vivarium at gestational day 6-8. Animals were kept in polycarbonate cages in a thermostatically controlled room at 21 ± 1 °C. The room was artificially illuminated from 6 a.m. to 6 p.m. The rats were fed conventional laboratory rat food (sniff R/M + H Spezieldiäten GmbH D-59494 Soest). All of the procedures conformed to the guidelines of the National Institutes of Health for the care and use of laboratory animals, were approved by the Local Ethical Committee of Gedeon Richter Plc. and were carried out in strict compliance with the European Directive 2010/63/EU regarding the care and use of laboratory animals for experimental procedures. All efforts were made to minimize the number of animals as well as their suffering. Experiments were performed and reported according to the ARRIVE guidelines on animal research.

Gestational valproic acid administration. The timed-pregnant female Sprague-Dawley rats received a single subcutaneous dose of 400 or 600 mg/kg sodium VPA (Sigma-Aldrich Chemical Co, UK) or vehicle (saline injection) in the loose skin area of the neck in a volume of 1 ml/kg dissolved in sterile physiological saline at gestational day 12.5 as described previously[59]. The treatment groups are referred to as VEH, VPA400 and VPA600. On postnatal day 21, male offspring were weaned and housed in groups of 3 or 4.

Age of the animals during the MRI experiments. During measurement 1 the animals were seven weeks old and during measurement 2 the animals were eleven weeks old. For weight, average in-scanner motion, isoflurane dose and respiration rate see Supplementary Table 1.

Image acquisition. Before magnetic resonance imaging, animals were habituated to the acoustic noise of the MRI scanner for 1 week in a separate animal room. In the experiments, 36 male rats (12 rats from each treatment group) were used. The mean (±standard deviation) initial weight of the rats was 209 (±27) g over the first MRI measurements (performed in a period of two weeks) and 393 (±23) g over the second MRI measurements (beginning one month after the end of the first measurement). Four rats were scanned per day in a random order from each treatment group.

On the day of scanning, rats were anesthetized before transporting to the magnet room. Anesthesia was introduced with 5% isoflurane and then maintained at approximately 1.25% during scanning. The body temperature was maintained at 38 ± 1 °C with thermostatically controlled air flow around the rat. The respiration of the animal was monitored continuously with a small pneumatic pillow sensor during the experiment (SA Instruments, Inc., NY, USA).

The MRI experiments were performed using a 9.4 T Varian MRI system (Varian Associates Inc., Palo Alto, CA) with a free bore size of 210 mm, which contained a 120 mm inner size gradient coil (minimum rise time 140 μs; 200 μs were used). For excitation, an actively RF-decoupled 2 channel volume coil system with an inner size of 70 mm was used, and a fixed-tuned receive-only phase array rat brain coil (RAPID Biomedical GmbH, Rimpar, Germany) was located directly above the dorsal surface of each rat's head to maximize the signal-to-noise ratio.

For the spatial coregistration of fMRI scans and for voxel-based morphometry (VBM), proton density weighted anatomical scans were acquired using gradient echo multi-slice imaging (GEMS; echo time (TE): 5.78 ms, repetition time (TR): 855 ms, flip angle: 40°, data matrix: 256 × 256, total scan time: 22 min 30 s) sequence with a field-of-view (FOV) of 40 mm × 40 mm and a slice thickness of 0.2 mm, without interslice gap. Seventy-four slices were acquired in an interleaved order. Anatomical scans were repeated 8 times and then averaged into a single image.

MRI measurements: anesthesia, respiration and motion. Since motion artifacts are very problematic in MRI, before any further analysis, we examined the magnitude and between-group differences in in-scanner motion, respiration and anesthetic dose. Despite the superficial anesthesia during functional MR imaging, motion was moderate throughout all MRI experiments (Supplementary Table 1). For both MRI measurements, weight, average in-scanner motion (as estimated by the motion correction algorithm), isoflurane dose and respiration rate were not different between the groups. Summary statistics of these measures are listed in Supplementary Table 1.

Functional MRI experiments. The T2*-weighted echo planar imaging (EPI) sequence for the fMRI experiments had the following settings: TE: 10 ms, TR: 2030 ms, flip angle: 90°, averages: 1, dummy scans: 4, data matrix: 50 × 50, 400 repetitions, FOV: 40 mm × 40 mm, slice thickness: 0.8 mm, no interslice gap, and 16 horizontal slices (resolution: 0.8 × 0.8 × 0.8 mm^3). For the reduction of the EPI Nyquist ghost artifact, a triple reference scan[60] was used, meaning that the functional images were acquired with two opposite gradient polarities, which resulted in an effective TR of 4060 ms.

For a somatosensory stimulus, pneumatic "air-puffed" whisker stimulation was used in a block-design fashion. The stimulation was delivered to the right whisker pad of the animals through a tubing system that was integrated into the holding cradle. The air pressure was set to 1 bar. Air puffs were delivered at a frequency of 1 Hz with a blowing time of 200 ms. The duration of the stimulation blocks was 30 s followed by a 60 s rest. Over one experimental session, 6 blocks of stimulation were used. The pneumatic stimulation was controlled by a custom-programmed user interface developed in LabView (National Instruments Corporation, Austin, TX, USA).

Exclusion criteria. Exclusion criteria were fixed prior to data analysis as follows: scans with striking imaging artifacts (based on visual inspection) or with an average root mean squared relative displacement greater than 0.05 mm during the fMRI scan (as calculated by FSL) were subject to exclusion from all analyses.

Moreover, subjects without immunohistological data were excluded from the analyses focusing on the correlation of BOLD response with Purkinje cell number and its group-level interaction.

None of the scans had to be discarded due to artifacts or in-scanner motion issues, resulting in N = 36 for the whole-brain fMRI analysis of the first measurement. On the other hand, in the second measurement, 3 animals had to be excluded because of in-scanner motion and inadequate anesthesia (2 controls and 1 in the VPA600 group), resulting in N = 33.

The immunohistology experiments were only performed for N = 9 animals per group, and one animal from the VPA600 group had to be excluded for technical reasons.

Imaging data analysis. To obtain maximally translatable results, we followed the conventions set for human MRI analysis, similar to our previous works[61,62]. Small-animal imaging-specific features of the applied image processing pipeline are described in detail. When not specified otherwise, the same data analysis steps were performed in the first and second MRI measurements.

Preprocessing. The raw images were converted to NIfTI-format (Neuroimaging Informatics Technology Initiative) by an in-house developed script. The anatomical and functional images were reoriented to match the standard orientation of the digitalized version of the Rat Brain Atlas of Paxinos and Watson[63]. All images were rescaled by a factor of ten to achieve image dimensions similar to human data and thus facilitate the use of image processing algorithms developed for human image analysis. All the approaches performed on the upscaled images were scale-invariant, except for a built-in constraint optimization for motion correction. The upscaling only affects the dimension descriptor fields in the file header and does not involve interpolation or any information loss. The analysis was carried out in a multistage process using the image analysis software package, FSL[64] (FMRIB's Software Library, www.fmrib.ox.ac.uk/fsl), and in-house developed software tools. All the fMRI time-series were motion-corrected using MCFLIRT[65]. FSL BET (Brain Extraction Tool[66]) was used to remove nonbrain areas from the structural and functional images. The fractional intensity threshold was set to 0.65 and 0.7 for functional and structural images, respectively, and the vertical gradient in the fractional threshold was set to 0.1. Before the brain extraction, the images were rescaled in the y-direction by a factor of 0.5 to ensure that the spherical brain model used by BET gained robust segmentation results. The brain-extracted images were then rescaled to the original y-axis dimensions.

To achieve spatial correspondence for the group analysis, all images were spatially standardized using FSL FLIRT[67], which utilized a 6-parameter rigid-body transformation. The high-resolution structural image was fitted to an in-house developed standard template[62] (average of 200 nonlinearly fitted structural images) by an affine transformation (FLIRT) and a nonlinear deformation field estimated by FNIRT[68]. In the latter coregistration procedure, a $10 \times 10 \times 10\,mm^3$ warping field (in upscaled space) was estimated with three iterations using a relatively conservative lambda parameter set of 60, 40 and 20. This stricter regularization was applied as the morphological diversity of the rat brain is smaller compared to humans.

Voxelwise functional MRI (fMRI) analysis. Before the statistical analysis, the functional images were spatially smoothed using a Gaussian kernel of 12.0 mm FWHM (note that the images were upscaled). High-pass temporal filtering (Gaussian-weighted least-squares straight line fitting, with sigma = 140.0 s) was then applied to remove slow drifts from the signal. The fMRI data processing was carried out using FEAT (FMRI Expert Analysis Tool) Version 6.00, part of FSL. After signal prewhitening (FILM), the first-level statistical analysis on the time-series was carried out using the general linear model with local autocorrelation correction[69]. The analysis modeled each individual rat's data from each session and included 7 explanatory variables in total: one regressor modeling the stimuli (convolved with a double-gamma canonical HRF), its temporal derivate, to account for slight differences in timing and 5 noise-ROI-based, CompCor[70] confounder variables. For each fMRI session, a noise ROI was delineated based on the temporal signal-to-noise ratio of the BOLD signals (the upper 2 percentiles of within-brain voxels were chosen on each slice), and the first five principal components of the corresponding time-series were extracted from the data, following the broadly used t-CompCor technique[70]. Individual statistical Z-score images for the first regressor were obtained (average BOLD response to the stimuli).

Using the spatial transformations computed during image coregistration and standardization, Z-score maps resulting from the individual statistical analysis were realigned to the common standard space to achieve spatial correspondence during the group-level voxelwise analysis.

A second-level general linear model analysis was performed with FEAT. Data from the first and second measurements were analyzed separately. Three different statistical models were evaluated for both measurements.

Model 1 was a simple model with three explanatory variables modeling the treatment groups with dummy coding (N = 36 and 33 for measurement 1 and 2, respectively). Statistical contrasts were defined to assess the VPA400 vs. VEH., VPA600 vs. VEH and VPA400 vs. VPA600 comparisons. An F-contrast was also specified to establish a statistical map of voxels activated in at least one of the three groups. This map was used for defining unbiased ROIs.

Model 2 was a model analogous to Model 1 but with the restricted population for which histological data were also available (N = 25, for both measurements). The goal of this model was simply to demonstrate that the results of model 1 are not driven by animals excluded from further analysis (that is, the restricted population is still representative in terms of findings in the whole population).

Model 3, next to the three explanatory variables of Model 2 (representing the VPA groups), involved three extra explanatory variables. Those represent the statistical interaction, by containing the demeaned (globally, for all included subjects), normalized Purkinje cell numbers of the cerebellar lobule 7, multiplied by the group-level explanatory variables, respectively. With the proper contrasts, this model allowed for analyzing the groupwise correlations between Purkinje cell number and BOLD response, as well as the interaction effects, comparing the regression slopes between groups (N = 25 for both measurements).

The resulting group-level statistical maps were corrected for multiple comparisons on the voxelwise-level, with a GRF-theory-based maximum height thresholding procedure and thresholded with a significance threshold of P = 0.05[71]. For the second measurement, a cluster-based thresholding was also applied, with a Z = 3.1 cluster-forming threshold and a cluster probability cutoff of P = 0.05. This thresholding method, although less effective in localizing the activation, was used because the voxelwise thresholding was too conservative for the observed lower effect sizes in the group-contrast images of measurement 2.

ROI analysis. In addition to voxel-based analyses, a cerebral and cerebellar ROI was defined, and the individual ROI-mean percent BOLD signal change was calculated and compared between groups. These ROIs were delineated based on the unbiased F-contrast of Model 1 to avoid favoring any of the groups. This activation map was thresholded with a GRF theory-based maximum height thresholding procedure and thresholded with a significance threshold of P = 0.05 to identify voxels that were activated in at least one of the groups. The resulting activation mask was than multiplied by in-house cerebellum and cerebrum masks to define the cerebellar

and cerebral ROIs of activation, respectively. These were used for the ROI-level interaction analysis (Fig. 6). These F-contrast based ROIs might not be the most sensitive way to extract information regarding the observed interaction-effect, but guarantee unbiased results and eliminate statistical pitfalls.

MRI volumetric and voxel-based morphometry analysis. We used the voxel-based morphometry (VBM)-style protocol[72] of FSL[66], but optimized for the rat brain, as in our previous study[61]. Nonbrain parts were removed from all the structural images[66], and tissue-type segmentation was carried out by FAST4[73]. To obtain optimal tissue classification, an in-house *a priori* tissue map[61] was used. The volume of whole-brain gray and white matter was estimated by taking the sum of the corresponding partial-volume estimate maps.

The resulting gray-matter partial volume images were registered to a standard space using linear transformation[65], followed by a nonlinear registration[68]. The resulting images were averaged to create a study-specific template, to which the native-space gray matter images were then nonlinearly reregistered. The registered partial volume images were then modulated (to correct for local expansion or contraction) by being divided with the Jacobian of the warp field (incorporating the linear scaling factor, as well). The modulated segmented images were then smoothed with an isotropic Gaussian kernel with a sigma of 4 mm. Finally, statistical inference on the treatment effect was performed by voxelwise GLM with permutation-based nonparametric testing (FSL's randomise). Cluster-based belief-boosting was carried out by the TFCE technique[74]. The images were then thresholded with permutation-based empirical maximum height thresholding at a (corrected) significance threshold of $P = 0.05$[71].

Histological processing. *Perfusion and preparation of tissue sections.* The animals were deeply anesthetized using intraperitoneal injection of an anesthetic mixture (containing ketamine, xylazine hydrochloride, promethazinium chloride) and perfused through the heart first with saline (2–3 min) followed by a fixative (30 min) containing 4% paraformaldehyde in 0.1 M phosphate buffer (PB) (pH 7.4). Brains were removed from the skull and the cerebella were dissected and then washed three times in PB. In all cases, sagittal slices from the cerebellar vermis were cut at a thickness of 60 μm with a vibratome. After vibratome slicing and extensive washing in 0.1 M PB, the 60 μm-thick sections were incubated in 30% sucrose overnight, followed by freeze thawing over liquid nitrogen four times.

Immunocytochemistry. The sections were processed for immunoperoxidase staining. All washing steps and dilutions of the antibodies were performed in 0.05 M Tris-buffered saline (TBS), pH 7.4. After extensive washing in TBS, the sections were blocked in 3% bovine serum albumin for 45 min and then incubated in rabbit anti-calbindin-D28kD antibody (1:1000, Swant) for a minimum of 48 h at 4 °C. Following the primary antisera, the sections were treated with biotinylated anti-rabbit IgG (1:300) raised in goat for 2 h and then with avidin biotinylated horseradish peroxidase complex (1:500; Elite ABC; Vector Laboratories) for 3 h at room temperature. The immunoperoxidase reaction was developed using 3,3′-diaminobenzidine (DAB) as the chromogen.

Purkinje cell quantification. The quantification of cerebellar Purkinje cells is based on the CB immunostained sagittal sections of the cerebellar vermis of 27 rats (9 from each animal group). In general, 8-10 sagittal sections were included in the Purkinje cell quantification per animal. Purkinje cells were quantified by counting CB+ cell bodies in the Purkinje layer of the entire lobule. After counting the Purkinje cells in a vermal cerebellar lobule, the length of the Purkinje cell layer in the lobule was traced and measured by ImageJ software (v1.50b). Then the number of Purkinje cells for the given layer (6a, 6b, 6c, 7) was calculated (count/length, traced layer) for 100 μm layer length.

Statistical analysis of brain volumetry, ROI and histological data. Gray and white matter volumetry, cerebral and cerebellar ROI and lobule-wise histological data were compared by means of permutation testing to overcome possible normality issues. Permutation-based linear models (R-package lmPerm) were fitted to explain these data with a factor variable representing the treatment groups. Additionally, for the interaction analysis of the cerebral and cerebellar ROIs, the demeaned, normalized Purkinje cell number of the cerebellar lobe 7, and its interaction with the group factor variable was also added.

The number of maximum permutations was set to 100000, and factor variables were explicitly set to be handled with the "treatment" contrast of R (traditional "dummy coding"). Permutations were stopped when the estimated standard error of the estimated p was less than 0.01*p.

Data Availability

Data generated and analysed during this study are included in this published article and its Supplementary Information material, the full datasets generated during and/or analysed during the current study are available from the corresponding author on reasonable request.

References

1. DSM-5. *American Psychiatric Association: Diagnostic and Statistical Manual of Mental Disorders* (2013).
2. Abraham, A. *et al.* Deriving reproducible biomarkers from multi-site resting-state data: An Autism-based example. *NeuroImage* **147**, 736–745 (2017).
3. Di Martino, A. *et al.* Enhancing studies of the connectome in autism using the autism brain imaging data exchange II. *Sci Data* **4**, 170010 (2017).
4. Syed, M. A., Yang, Z., Hu, X. P. & Deshpande, G. Investigating Brain Connectomic Alterations in Autism Using the Reproducibility of Independent Components Derived from Resting State Functional MRI Data. *Front Neurosci* **11**, 459 (2017).
5. Shen, M.D. *et al.* Increased Extra-axial Cerebrospinal Fluid in High-Risk Infants Who Later Develop Autism. *Biol Psychiatry* (2017).
6. Amaral, D. G., Schumann, C. M. & Nordahl, C. W. Neuroanatomy of autism. *Trends Neurosci* **31**, 137–145 (2008).
7. D'Mello, A. M., Crocetti, D., Mostofsky, S. H. & Stoodley, C. J. Cerebellar gray matter and lobular volumes correlate with core autism symptoms. *Neuroimage Clin* **7**, 631–639 (2015).
8. D'Mello, A. M. & Stoodley, C. J. Cerebro-cerebellar circuits in autism spectrum disorder. *Front Neurosci* **9**, 408 (2015).

9. Allen, G. & Courchesne, E. Differential effects of developmental cerebellar abnormality on cognitive and motor functions in the cerebellum: an fMRI study of autism. *Am J Psychiatry* **160**, 262–273 (2003).
10. Mosconi, M. W., Wang, Z., Schmitt, L. M., Tsai, P. & Sweeney, J. A. The role of cerebellar circuitry alterations in the pathophysiology of autism spectrum disorders. *Front Neurosci* **9**, 296 (2015).
11. Stoodley, C. J. *et al*. Altered cerebellar connectivity in autism and cerebellar-mediated rescue of autism-related behaviors in mice. *Nature neuroscience* **20**, 1744–1751 (2017).
12. Fatemi, S. H. *et al*. Consensus paper: pathological role of the cerebellum in autism. *Cerebellum* **11**, 777–807 (2012).
13. Skefos, J. *et al*. Regional alterations in purkinje cell density in patients with autism. *PloS one* **9**, e81255 (2014).
14. Clifford, H., Dulneva, A., Ponting, C. P., Haerty, W. & Becker, E. B. E. A gene expression signature in developing Purkinje cells predicts autism and intellectual disability co-morbidity status. *Sci Rep* **9**, 485 (2019).
15. Kelly, R. M. & Strick, P. L. Cerebellar loops with motor cortex and prefrontal cortex of a nonhuman primate. *J Neurosci* **23**, 8432–8444 (2003).
16. Schmahmann, J. D. The cerebellum and cognition. *Neurosci Lett* (2018).
17. Allen, G., Buxton, R. B., Wong, E. C. & Courchesne, E. Attentional activation of the cerebellum independent of motor involvement. *Science* **275**, 1940–1943 (1997).
18. Salmi, J. *et al*. Cognitive and motor loops of the human cerebro-cerebellar system. *J Cogn Neurosci* **22**, 2663–2676 (2010).
19. Timmann, D. & Daum, I. Cerebellar contributions to cognitive functions: a progress report after two decades of research. *Cerebellum* **6**, 159–162 (2007).
20. Schmahmann, J. D. From movement to thought: anatomic substrates of the cerebellar contribution to cognitive processing. *Human brain mapping* **4**, 174–198 (1996).
21. Badura, A. *et al*. Normal cognitive and social development require posterior cerebellar activity. *Elife* **7** (2018).
22. Wang, S. S., Kloth, A. D. & Badura, A. The cerebellum, sensitive periods, and autism. *Neuron* **83**, 518–532 (2014).
23. Diamond, M. E., von Heimendahl, M., Knutsen, P. M., Kleinfeld, D. & Ahissar, E. Where and what in the whisker sensorimotor system. *Nat Rev Neurosci* **9**, 601–612 (2008).
24. Tsurugizawa, T., Takahashi, Y. & Kato, F. Distinct effects of isoflurane on basal BOLD signals in tissue/vascular microstructures in rats. *Sci Rep* **6**, 38977 (2016).
25. Sandin, S. *et al*. The familial risk of autism. *Jama* **311**, 1770–1777 (2014).
26. Schneider, T. & Przewlocki, R. Behavioral alterations in rats prenatally exposed to valproic acid: animal model of autism. *Neuropsychopharmacology: official publication of the American College of Neuropsychopharmacology* **30**, 80–89 (2005).
27. Mabunga, D. F., Gonzales, E. L., Kim, J. W., Kim, K. C. & Shin, C. Y. Exploring the Validity of Valproic Acid Animal Model of Autism. *Exp Neurobiol* **24**, 285–300 (2015).
28. Nicolini, C. & Fahnestock, M. The valproic acid-induced rodent model of autism. *Exp Neurol* (2017).
29. Ingram, J. L., Peckham, S. M., Tisdale, B. & Rodier, P. M. Prenatal exposure of rats to valproic acid reproduces the cerebellar anomalies associated with autism. *Neurotoxicology and teratology* **22**, 319–324 (2000).
30. Main, S. L. & Kulesza, R. J. Repeated prenatal exposure to valproic acid results in cerebellar hypoplasia and ataxia. *Neuroscience* (2016).
31. Al Sagheer, T. *et al*. Motor Impairments Correlate with Social Deficits and Restricted Neuronal Loss in an Environmental Model of Autism. *The international journal of neuropsychopharmacology/official scientific journal of the Collegium Internationale Neuropsychopharmacologicum* **21**, 871–882 (2018).
32. Roux, S., Bailly, Y. & Bossu, J. L. Regional and sex-dependent alterations in Purkinje cell density in the valproate mouse model of autism. *Neuroreport* **30**, 82–88 (2019).
33. Frisch, C. *et al*. Dose-dependent memory effects and cerebral volume changes after in utero exposure to valproate in the rat. *Epilepsia* **50**, 1432–1441 (2009).
34. Wegiel, J. *et al*. Contribution of olivofloccular circuitry developmental defects to atypical gaze in autism. *Brain Res* **1512**, 106–122 (2013).
35. Pierce, K. & Courchesne, E. Evidence for a cerebellar role in reduced exploration and stereotyped behavior in autism. *Biol Psychiatry* **49**, 655–664 (2001).
36. Jung, M. *et al*. Default mode network in young male adults with autism spectrum disorder: relationship with autism spectrum traits. *Mol Autism* **5**, 35 (2014).
37. Verly, M. *et al*. Altered functional connectivity of the language network in ASD: role of classical language areas and cerebellum. *Neuroimage Clin* **4**, 374–382 (2014).
38. Favre, M. R. *et al*. General developmental health in the VPA-rat model of autism. *Frontiers in behavioral neuroscience* **7**, 88 (2013).
39. Go, H. S. *et al*. Prenatal exposure to valproic acid increases the neural progenitor cell pool and induces macrocephaly in rat brain via a mechanism involving the GSK-3beta/beta-catenin pathway. *Neuropharmacology* **63**, 1028–1041 (2012).
40. Bernhardt, B. C., Di Martino, A., Valk, S. L. & Wallace, G. L. Neuroimaging-Based Phenotyping of the Autism Spectrum. *Curr Top Behav Neurosci* **30**, 341–355 (2017).
41. Wallace, G. L. *et al*. Longitudinal cortical development during adolescence and young adulthood in autism spectrum disorder: increased cortical thinning but comparable surface area changes. *J Am Acad Child Adolesc Psychiatry* **54**, 464–469 (2015).
42. van Rooij, D. *et al*. Cortical and Subcortical Brain Morphometry Differences Between Patients With Autism Spectrum Disorder and Healthy Individuals Across the Lifespan: Results From the ENIGMA ASD Working Group. *Am J Psychiatry*, appiajp201717010100 (2017).
43. Valk, S. L., Di Martino, A., Milham, M. P. & Bernhardt, B. C. Multicenter mapping of structural network alterations in autism. *Human brain mapping* **36**, 2364–2373 (2015).
44. Carper, R. A. & Courchesne, E. Inverse correlation between frontal lobe and cerebellum sizes in children with autism. *Brain* **123**(Pt 4), 836–844 (2000).
45. Carper, R. A. & Courchesne, E. Localized enlargement of the frontal cortex in early autism. *Biol Psychiatry* **57**, 126–133 (2005).
46. Miyazaki, M. *et al*. Short-latency somatosensory evoked potentials in infantile autism: evidence of hyperactivity in the right primary somatosensory area. *Developmental medicine and child neurology* **49**, 13–17 (2007).
47. Zhang, Y. *et al*. Dendritic channelopathies contribute to neocortical and sensory hyperexcitability in Fmr1(−/y) mice. *Nature neuroscience* **17**, 1701–1709 (2014).
48. Dendrinos, G., Hemelt, M. & Keller, A. Prenatal VPA Exposure and Changes in Sensory Processing by the Superior Colliculus. *Frontiers in integrative neuroscience* **5**, 68 (2011).
49. Dubiel, A. & Kulesza, R. Prenatal valproic acid exposure disrupts tonotopic c-Fos expression in the rat brainstem. *Neuroscience* **311**, 349–361 (2015).
50. Coskun, M. A., Loveland, K. A., Pearson, D. A., Papanicolaou, A. C. & Sheth, B. R. Functional assays of local connectivity in the somatosensory cortex of individuals with autism. *Autism research: official journal of the International Society for Autism Research* **6**, 190–200 (2013).
51. Hegarty, J. P. 2nd, Weber, D. J., Cirstea, C. M. & Beversdorf, D. Q. Cerebro-Cerebellar Functional Connectivity is Associated with Cerebellar Excitation-Inhibition Balance in Autism Spectrum Disorder. *Journal of autism and developmental disorders* (2018).
52. Khan, A. J. *et al*. Cerebro-cerebellar Resting-State Functional Connectivity in Children and Adolescents with Autism Spectrum Disorder. *Biol Psychiatry* **78**, 625–634 (2015).

53. Oldehinkel, M. *et al*. Altered Connectivity Between Cerebellum, Visual, and Sensory-Motor Networks in Autism Spectrum Disorder: Results from the EU-AIMS Longitudinal European Autism Project. *Biol Psychiatry Cogn Neurosci Neuroimaging* (2018).
54. Ramos, T. C., Balardin, J. B., Sato, J. R. & Fujita, A. Abnormal Cortico-Cerebellar Functional Connectivity in Autism Spectrum Disorder. *Front Syst Neurosci* **12**, 74 (2018).
55. Thomsen, K., Piilgaard, H., Gjedde, A., Bonvento, G. & Lauritzen, M. Principal cell spiking, postsynaptic excitation, and oxygen consumption in the rat cerebellar cortex. *J Neurophysiol* **102**, 1503–1512 (2009).
56. Howarth, C., Gleeson, P. & Attwell, D. Updated energy budgets for neural computation in the neocortex and cerebellum. *J Cereb Blood Flow Metab* **32**, 1222–1232 (2012).
57. Roux, S., Lohof, A., Ben-Ari, Y., Poulain, B. & Bossu, J. L. Maturation of GABAergic Transmission in Cerebellar Purkinje Cells Is Sex Dependent and Altered in the Valproate Model of Autism. *Front Cell Neurosci* **12**, 232 (2018).
58. Kuo, H. Y. & Liu, F. C. Molecular Pathology and Pharmacological Treatment of Autism Spectrum Disorder-Like Phenotypes Using Rodent Models. *Front Cell Neurosci* **12**, 422 (2018).
59. Kim, K. C. *et al*. The critical period of valproate exposure to induce autistic symptoms in Sprague-Dawley rats. *Toxicology letters* **201**, 137–142 (2011).
60. van der Zwaag, W. *et al*. Minimization of Nyquist ghosting for echo-planar imaging at ultra-high fields based on a "negative readout gradient" strategy. *J Magn Reson Imaging* **30**, 1171–1178 (2009).
61. Nyitrai, G. *et al*. Stepwise occlusion of the carotid arteries of the rat: MRI assessment of the effect of donepezil and hypoperfusion-induced brain atrophy and white matter microstructural changes. *PloS one* **13**, e0198265 (2018).
62. Spisak, T. *et al*. Central sensitization-related changes of effective and functional connectivity in the rat inflammatory trigeminal pain model. *Neuroscience* **344**, 133–147 (2017).
63. Paxinos, G. & Watson, C. eds *The Rat Brain in Stereotaxic Coordinates* (Elsevier Academic Press, Burlington, M. A., 2005).
64. Jenkinson, M., Beckmann, C. F., Behrens, T. E., Woolrich, M. W. & Smith, S. M. Fsl. *NeuroImage* **62**, 782–790 (2012).
65. Jenkinson, M., Bannister, P., Brady, M. & Smith, S. Improved optimization for the robust and accurate linear registration and motion correction of brain images. *NeuroImage* **17**, 825–841 (2002).
66. Smith, S. M. Fast robust automated brain extraction. *Human brain mapping* **17**, 143–155 (2002).
67. Jenkinson, M. & Smith, S. A global optimisation method for robust affine registration of brain images. *Medical image analysis* **5**, 143–156 (2001).
68. Andersson, J. L. R., Jenkinson, M. & Smith, S. Non-linear optimisation. In *FMRIB technical report* (Oxford, 2007).
69. Woolrich, M. W., Ripley, B. D., Brady, M. & Smith, S. M. Temporal autocorrelation in univariate linear modeling of FMRI data. *NeuroImage* **14**, 1370–1386 (2001).
70. Behzadi, Y., Restom, K., Liau, J. & Liu, T. T. A component based noise correction method (CompCor) for BOLD and perfusion based fMRI. *NeuroImage* **37**, 90–101 (2007).
71. Worsley, K. J. Statistical analysis of activation images. in *Functional MRI: An Introduction to Methods* (eds Jezzard, P., Matthews, P. M. & Smith, S. M.) 251–271 (Oxford Universtiy Press, Oxford, 2001).
72. Ashburner, J. & Friston, K. J. Voxel-based morphometry–the methods. *Neuroimage* **11**, 805–821 (2000).
73. Zhang, Y., Brady, M. & Smith, S. Segmentation of brain MR images through a hidden Markov random field model and the expectation-maximization algorithm. *IEEE transactions on medical imaging* **20**, 45–57 (2001).
74. Smith, S. M. & Nichols, T. E. Threshold-free cluster enhancement: addressing problems of smoothing, threshold dependence and localisation in cluster inference. *Neuroimage* **44**, 83–98 (2009).

Acknowledgements

The authors are thankful to Prof. Dagmar Timmann-Braun for her most valuable insights regarding the interpretation of the cerebrocerebellar aspects of our results. The authors are also grateful for the technical assistance of Anita Bérces, Tiborné Gyarmati, Pálma Diószegi and Katalin Tóthné Fekete. This work was supported by Gedeon Richter Plc. and the Hungarian National Research, Development and Innovation Office (KMOP-1.1.5-08-2009-0001, ERNYO-13-1-2013-0003).

Author Contributions

T.S., V.R., G.É.Ny., Gy.L., L.B., E.P. and A.Cz. designed the experiments. R.K., K.S., C.K.Cs., A.V., D.G. and E.P. performed the experiments. T.S., V.R., G.É.Ny., Zs.S., E.P. and Zs.T.K. analysed the data. T.S., V.R. and A.Cz. wrote the main manuscript text and T.S. and E.P. prepared figures. All authors reviewed the manuscript.

Additional Information

Supplementary information accompanies this paper at https://doi.org/10.1038/s41598-019-45667-1.

Competing Interests: T.S., V.R., R.K., K.S., C.K.Cs., A.V., D.G., G.É.Ny., Zs.S., Gy.L., L.B. and A.Cz. are employees of Gedeon Richter Plc., or were full time employees of that firm at the time the research was performed. This does not alter our adherence to Sci Rep policies on sharing data and materials. The remaining authors, E.P. and Zs.T.K., declare no potential conflict of interest.

Publisher's note: Springer Nature remains neutral with regard to jurisdictional claims in published maps and institutional affiliations.